Atmospheric Optical Calibration System for Outdoor Testing of Photovoltaic Devices

T. W. Cannon and R. L. Hulstrom

Abstract. The Atmospheric Optical Calibration System (AOCS) was developed at the National Renewable Energy Laboratory for making real-time, terrestrially based measurements of selected optical properties of the atmosphere. The original application of the AOCS was to provide measurements of atmospheric optical conditions pertinent to outdoor photovoltaic (PV) device performance measurements. It addresses the dependence of outdoor PV test results on the characteristics of the incident solar radiation that are dependent on these constantly changing atmospheric optical conditions. This paper describes the AOCS, its calibration and its application to PV testing. Additional applications related to the measurement of atmospheric optical properties are also mentioned.

1. Introduction

Photovoltaic (PV) devices are tested outdoors because: (a) the outdoors represents the physical and optical environment in which PV systems are used; and (b) it is generally difficult to test PV modules, panels or systems using solar simulators because these would be prohibitively large and expensive to operate continuously. A significant disadvantage of outdoor testing is that the properties of the radiation are dynamic; i.e. the total solar irradiance, spectral shape and spatial distribution are continuously changing due to changes in the slant path of the direct-beam sunlight through the atmosphere (i.e. the relative air mass), the content of atmospheric gases, aerosol particles, water vapour and clouds, and ground reflectance as viewed by the device [1]. Various investigators [2-4] have shown that atmospheric optical parameters and the resultant spectral solar irradiance incident on a PV device are significant determinants of its performance characteristics (e.g. short-circuit current, fill factor, efficiency and power output). Methods of dealing with these changes are to use reference solar cells [5], spectral corrections from measurements of the solar spectra [6], or a spectral model driven by meteorological conditons [7] to adjust the PV data. Each of these methods has its own shortcomings [8].

T. W. Cannon and R. L. Hulstrom: National Renewable Energy Laboratory, Golden, CO 80401, USA.

The AOCS provides a new, patented [9] approach in which certain atmospheric optical properties are measured concurrently with the PV measurements. The AOCS measurements are then used to define parameters for the atmospheric optical conditions; these parameters can subsequently be used to analyse and adjust the PV data. This paper describes the instrument, its calibration and its application to some preliminary PV measurements.

2. The Measured Optical Properties

We have selected the atmospheric optical properties listed in Table 1 for measurement using the AOCS.

As discussed by Iqbal [10], the effect of Rayleigh scattering can be calculated from the pressure-corrected air mass and the Rayleigh spectral attenuation coefficients.

The narrowband channel wavelengths chosen for the aerosol scattering and absorption measurements are selected World Meteorological Organization (WMO) standard wavelengths for determining atmospheric transmission in the UVA (0,368 μm), visible (0,500 μm) and NIR (0,862 μm) [11]. The range 0,4 μm to 0,7 μm was chosen for broadband absorption and scattering measurements because measurements in this band are essentially independent of water vapour (which is measured independently), yet

Table 1. Optical properties measured by the AOCS.

Property	Measurement
Molecular scattering	Surface pressure
Aerosol scattering and absorption	Aerosol optical depth at 0,368 μm, 0,500 μm and 0,862 μm
	Ratio of diffuse- to global-horizontal photon flux densities, 0,4 μm to 0,7 μm
Water-vapour absorption	Ratio of direct-beam irradiance at 0,862 μm to that at 0,942 μm

they are strongly dependent on atmospheric absorption and scattering. Commercial quantum sensors filtered to measure photon flux over this region were readily available.

Atmospheric precipitable water vapour is calculated from the ratio of direct-beam irradiance at 0,942 μm (a water-vapour absorption band) to the irradiance at 0,862 μm (a water-vapour window) [12] using the method described in Section 5 of this paper.

3. Instrumentation

The AOCS consists of four basic physical components: direct-beam module (DBM) with solar tracker, global-horizontal module, plane-of-array module, and a computer system for data acquisition and control.

There are ten optical channels, as described in Table 2. The optical channels of primary interest are the narrow-beam, narrow field-of-view (FOV) (channels 0 to 3) at the WMO standard wavelengths; direct-beam, quantum sensor (channel 5), all housed in the DBM; and the global-horizontal quantum sensor (channel 7) attached to the global-horizontal module plate.

Four additional sensors are used to check certain calculations made by the AOCS computer program: a pyrheliometer (channel 4), global-horizontal and plane-of-array pyranometers (channels 6 and 8, respectively), and a plane-of-array quantum sensor (channel 9).

The narrowband (0,010 μm bandpass) channels have a 2,3° FOV with a collimation ratio (length-to-entry port diameter ratio) of 25. Both broadband, direct-beam channels have the same geometrical parameters as the Eppley Normal Incidence Pyrheliometer (NIP) (5,7° FOV and collimation ratio of 10).

A front view of the DBM is shown in Figure 1. In the photograph, the small (upper) cylinder contains the direct-beam quantum sensor channel; the large

cylinder contains the four narrow-beam channels and the pyrheliometer. Each optical channel consists of a sapphire window, three apertures that define the beam geometry, optical filters (except channel 4), and silicon detector/operational amplifier combination (channels 0 to 3) or silicon detectors with separate operational amplifiers (channels 4 to 9). The large cylinder also contains a data logger with a 10-bit (1:1024) analogue-to-digital converter. Refillable, indicating desiccant cartridges are used in both cylinders for humidity control. To prevent pooling of moisture on the outside of the windows, the sapphire windows are flush mounted. The DBM is waterproof, as tested by submersion in water.

A PC-type computer is used to control the AOCS and process the data. Communication between the computer and the AOCS is via a RS-232C serial bus at 300 baud.

4. Calibration

The four narrowband optical channels (0,368 μm, 0,500 μm, 0,862 μm and 0,942 μm) were calibrated using the Langley plot method [13]. Measurements were made every 5 minutes on six predominantly cloud-free days. To determine the calibration value V_{0ij} for channel i, day j, a straight-line fit of the natural logarithm of signal [ln (V_{ij})] versus relative air mass (RAM) was extrapolated to the calibration value, i.e. the air mass zero intercept [ln (V_{0ij})].

Langley data characteristically depart from linearity due to changes in atmospheric composition throughout the day. Considerable reduction in the uncertainty of ln (V_{0ij}) can be obtained using statistical analyses. Two techniques were used: (a) removal of selected outliers using the modified Thompson-τ technique; and (b) use of weighted averages to calculate an average ln (V_{0i}). These methods are described in [14].

Briefly, the Thompson-τ technique compares the largest outlier d with the product τS_{ij}, where τ has a value dependent on the number of data N_j ($\tau = 1,924$ for $N_j \geq 40$ at the 5 % significance level*) and S_{ij} is the standard deviation of the outlier values from a linear fit to the data. If $d \geq \tau S_{ij}$, then ln (V_{ij}) is considered an outlier and is eliminated. Outliers are eliminated one at a time, followed by a recalculation of the fit, until no more outliers are identified.

As an example, Figure 2 shows a Langley plot for the 0,5 μm channel taken on 11 February 1991. The dots correspond to the accepted data, the squares to the rejected.

Subsequent to Thompson-τ analysis, a weighted average for all of the runs was calculated. Weighting functions proportional to the reciprocal of the square

---

* The probability of rejecting good points is limited to 5 %.

Table 2. Optical channels.

Channel number/identity	Wavelength(s)/μm	Bandpass/μm	Field-of-view/°	Used to calculate
Direct-beam module (DBM)				
0	0,368	0,010	2,3	Aerosol optical depth
1	0,500	0,010	2,3	Aerosol optical depth
2	0,862	0,010	2,3	Aerosol optical depth
3	0,942	0,010	2,3	Water-vapour absorption from the ratio of Channel 3 to Channel 2
4 DNPS	0,3 to 1,1	See note	5,7	Total DN irradiance flux (see below)
5 DNQS	0,4 to 0,7	See note	5,7	Total DN quantum flux (see below)
Global-horizontal module				
6 GHPS	0,3 to 1,1	See note	180	With Channel 4, total global-horizontal diffuse irradiance
7 GHQS	0,4 to 0,7	See note	180	With Channel 5, ratio of diffuse skylight photon flux density to global-horizontal photon flux density
Plane-of-array module				
8 GTPS	0,3 to 1,1	See note	180	Total global irradiance in tilt plane
9 GTQS	0,4 to 0,7	See note	180	Total photon flux in tilt plane

Note: Channels 5, 7 and 9 are filtered to give a signal proportional to the total photon flux, channels 4, 6 and 8 are unfiltered.
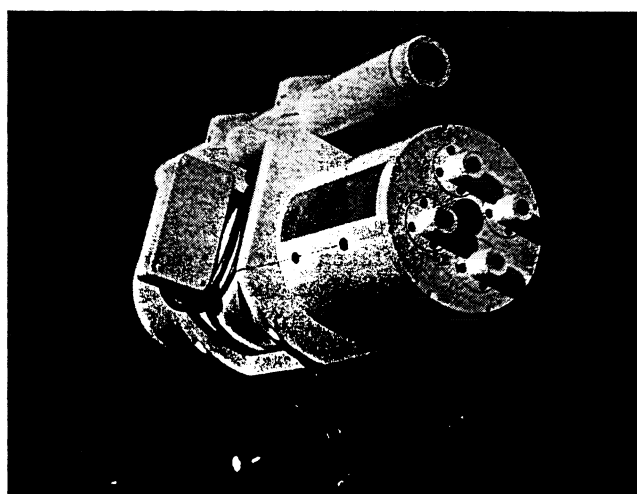
Figure 1. The AOCS direct-beam module. The four small apertures are the narrowband channels at 0,368 μm, 0,500 μm, 0,862 μm and 0,942 μm; the large-apertured channel in the large cylinder is the pyrheliometer, and the large aperture in the small cylinder is the quantum sensor pyrheliometer.
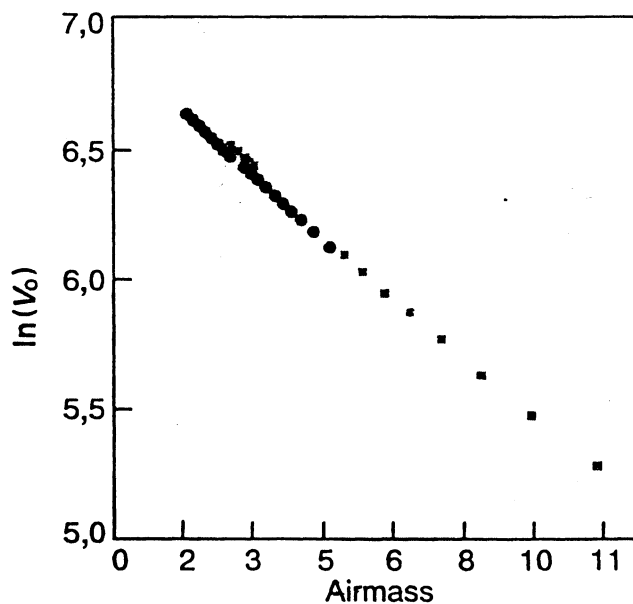
Figure 2. An AOCS Langley plot for one day of 0,500 μm data. The dots represent data accepted subsequent to Thompson-τ statistical analysis, the squares are the rejected data.

of the standard deviation on the data remaining after Thompson-τ analysis for each day were used. The weighted mean of $\ln(V_{0i})$ from N days of data is

$$\overline{\ln(V_{0i})} = \sum_{j=1}^{N} w_{ij} \overline{\ln(V_{0ij})}, \qquad (1)$$

where the weighting factors w_{ij} are given by

$$w_{ij} = \frac{\left(\dfrac{1}{S_{ij}}\right)^2}{\sum_{j=1}^{N} \left(\dfrac{1}{S_{ij}}\right)^2} \qquad (2)$$

for each average $\overline{\ln(V_{0ij})}$ with standard deviation S_{ij}.

Using this technique, averages with low values of standard deviation are weighted significantly more than those with higher standard deviations.

Table 3. Comparison of calibration value $\ln(V_{02})$ for Langley plots, AOCS 0,500 μm channel from six predominantly clear-sky cases.

	Before statistical analysis	After statistical analysis
Average, V_{02}	6,717	6,868
Weighted average	n/a	6,870
Precision index of average (PI)	0,274	0,001 25
Percentage PI	4,08	0,018 2
Number of data points	589	399

Table 3 illustrates the effectiveness of the method for reducing the uncertainty in the calibration. The table shows the intercept $\ln(V_{02})$, standard deviation (S_2) and number of data points (N_2) prior and subsequent to statistical analysis. Precision index (PI) is an estimate of the standard deviation.

Note the significant reduction in PI by elimination of 190 outliers using the technique. There is no indication of monotonic temporal drift over the 13-month period over which the data were taken.

Similar results were obtained for all of the narrowband channels.

The broadband optical channels ($i = 5$ to 10) were calibrated outdoors against the reference instruments. The direct-normal pyrheliometer channel (DNPS, $i = 5$) was calibrated against a reference Eppley Precision Spectral Pyranometer (PSP); the direct-normal quantum sensor (DNQS, $i = 6$) against a reference quantum sensor, with a 5,7° FOV direct-beam occultation, which had been calibrated against a NIST spectral-irradiance lamp standard in the NREL optics laboratory. The global-horizontal and global-tilt pyranometers (GHPS, $i = 7$, and GTPS, $i = 9$, respectively) were calibrated against a reference PSP and the global-horizontal and global-tilt quantum sensors (GHQS, $i = 8$, and GTQS, $i = 10$, respectively) were

calibrated against a second calibrated reference quantum sensor. The final calibration values are shown in Table 4 and are based on six calibration days, 17 January through 9 October 1990, under clear and partly cloudy skies.

The temperature and atmospheric pressure channels ($i = 11$ to 12, respectively) were calibrated by the National Renewable Energy Laboratory against reference instruments.

All direct-beam channel calibrations can be checked in the laboratory using the Sunphotometer Laboratory Calibration Facility (SLCF). This instrument, which was developed at the NREL, provides a very stable, intense and well-collimated light source for checking both the narrowband and broadband direct-beam channels. Positioning jigs are used to assure repeatability of the location of the AOCS relative to the source. Prior to each measurement, the output at the four narrowband wavelengths is checked using a set of reference narrowband filters and a silicon detector; these filters are measured on a Cary 2400 photometer to check for changes in throughput, bandwidth and peak-transmission wavelength. During the AOCS tests, the optical output of the SLCF is checked for stability using a broadband silicon detector.

The temperature response of all of the AOCS narrowband optical channels was measured in the laboratory. The DBM was placed in a styrofoam container and cooled to about $-12\,°C$ using dry ice. Electrical heater tape encircling the DBM was then energized to bring the unit slowly up to about $\pm 50\,°C$ while taking response data each minute with the test channel illuminated by the SLCF. The temperature coefficients are shown in Table 5.

Uncertainties in α are estimated to be $\pm 5\,\%$. The manufacturer's stated temperature coefficient for the broadband channel detectors is $< 1,5 \times 10^{-3}\,°C^{-1}$.

The geometrical properties of the direct-beam channels were measured using a "walk-through" test. The DBM were positioned about 4,5° ahead of the Sun on the AOCS polar tracker. Tracking was then terminated and data taken every 15 seconds during transit of the Sun. The data shown in Figure 3 for one narrow FOV and one broadband FOV channel were used to measure the FOVs and collimation ratios. See Chapter 5 of [15] for a description of sky-occluding geometries and the angle definitions. The results of the walk-through tests are shown in Table 6.

## 5. Derivation of the Precipitable Water Vapour Coefficients

An equation for precipitable water vapour (PWV) as a function of atmospheric optical transmission can be derived from the fundamental equations of optical

Table 4. Calibration factors for the broadband channels.

Channel number	Channel	Calibration factor	Standard deviation	Percentage standard deviation
5	DNPS	1,135	0,016	1,408
6	DNQS	$2,672 \times 10^{18}$	$0,083 \times 10^{18}$	3,089
7	GHPS	1,351	0,041	3,066
8	GHQS	$1,546 \times 10^{18}$	$0,013 \times 10^{18}$	0,873
9	GTPS	2,313	0,069	2,989
10	GTQS	$1,549 \times 10^{18}$	$0,008 \times 10^{18}$	0,526

Table 5. Temperature coefficients (α) of the narrowband optical channels based on SLCF measurements.

Channel number	Identity	α
0	0,368 μm	$-1,69 \times 10^{-4}$ °C^{-1}
1	0,500 μm	$-4,11 \times 10^{-4}$ °C^{-1}
2	0,862 μm	$1,27 \times 10^{-3}$ °C^{-1}
3	0,942 μm	$-2,99 \times 10^{-3}$ °C^{-1}
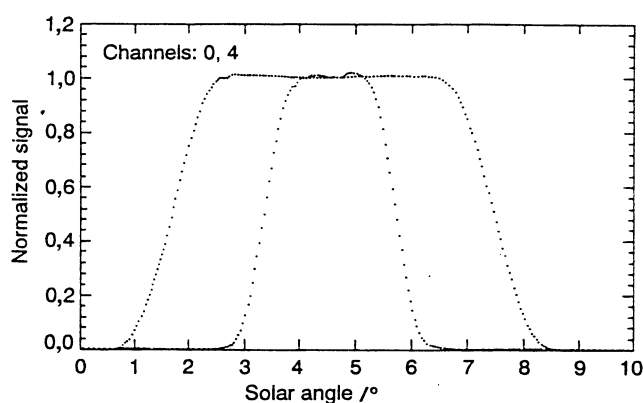
Figure 3. Walk-through test data on the 0,368 μm, narrow field-of-view, and the direct-normal pyrheliometer channels.

transmission. If exponential decay of the atmospheric pressure $p(h)$, water vapour density $\rho(h)$, and pressure-temperature $T(h)$ correction with height above reference (h) are assumed, i.e.

$$p(h) = p_0 \exp(-c_1 h) \tag{3}$$

$$\rho_w(h) = \rho_0 \exp(-c_2 h) \tag{4}$$

$$\frac{p(h)}{p(0)} \left(\frac{T(0)}{T(h)} \right)^{1/2} = \exp(-c_3 h), \tag{5}$$

then it can be shown that

$$W_v = \frac{1}{\text{RAM}} \frac{1}{\text{K5}} \left(\frac{p}{p_0} \right)^k \left[\ln \left(\text{K3} \frac{\text{V862}}{\text{V942}} \right) \right]^{\text{N3}}, \tag{6}$$

where W_v = the PWV in cm in the vertical direction, $p_0 = 101,3$ kPa, V862 = the AOCS signal at 0,862 μm, V942 = the AOCS signal at 0,942 μm and K3 is the ratio V942/V862 under extraterrestrial conditions, i.e. V_0942/V_0862.

Using values of the constants derived from atmospheric models (see Iqbal [10] for c_1 and McClatchey [16] for c_2 and c_3),

$$c_1 = 0,1184$$
$$c_2 = 0,439$$
$$c_3 = 0,126,$$

the derived values for K5, k and N3 are shown in the second column (model) of Table 7.

Table 6. Measured and design geometrical properties of the direct-beam channels.

Channel number	Sensor/μm	Slope angle/°	Limit angle/°	FOV/°	*AIM/°
0	0,368	0,93	1,73	2,7	0,000
1	0,500	0,93	1,65	2,6	0,000
2	0,862	0,92	1,75	2,7	0,000
3	0,942	0,90	1,70	2,6	+0,125
	WMO design	0,80	1,50	2,3	0,000
4	Pyranometer	2,10	3,90	6,0	+0,125
5	Quantum sensor	2,40	3,60	6,0	0,000
	Design	2,08	3,70	5,7	0,000

* AIM is the angle between each optical axis and the optical axis of the 0,5 μm channel, based on the centre of the plateau of each channel; + indicates that the aimpoint is clockwise from the 0,5 μm channel.

In order to determine K5, k and N3 and their uncertainties more realistically for the Denver area, sounding data from the National Weather Service facility at Stapleton International Airport for one year (1989) were used to calculate W_v by integration of water vapour over the path of the sonde; the corresponding values of atmospheric transmission at 0,862 µm and 0,942 µm can be calculated directly from optical transmission theory [12].

Writing (6) in the form

$$y = a_0 + a_1 x_1 + a_2 x_2,$$ (7)

where

$$y = \ln(RAM \times W_v)$$
$$a_0 = -\ln K5$$
$$a_1 = k$$
$$a_2 = N3$$
$$x_1 = \ln(p/p_0)$$
$$x_2 = \ln[-\ln \tau_{w942}].$$

assuming $V862/V_0 862 = 1$ in the optical window, and $\tau_{w942} = 942/V_0 942$, we can solve the matrix equation

$$Y = AX,$$ (8)

where Y represents the integrated PWV data from the soundings, A the coefficient matrix and X the calculated values x_1 and x_2. The method of LU decomposition and back substitution [17] together with an error estimation routine were written to solve this equation for A (i.e. a_0, a_1 and a_2). The final coefficient values are shown in Table 7 along with the original values and the values from the model.

The K3 values are instrument-dependent, i.e. they depend on the detector sensitivities, filter transmission factors, and amplifier gains for the two channels; one would not expect the model K3 value to be the same as that for the actual instrument. On the other hand, it is gratifying that the other two K3 values agree well, as they are derived using quite different methods. The value of k is sensitive to the vertical $p(h)$ profile. The difference in values shown

Table 7. Constants for the precipitable water vapour equation determined by various methods.

Constant	Model	Original value[b]	New value
K3	0,807[a]	0,506	0,545[c]
K5	0,44	0,254	0,25[d]
k	−2,54	−0,960	−1,19[d]
N3	1,8	1,82	1,9[d]

a. Based on the ratio of the extraterrestrial spectral irradiance value at 0,942 µm to that at 0,862 µm.
b. Based on optical transfer of a three-site sunphotometer calibration against microwave radiometers.
c. From the AOCS Langley plots at 0,862 µm and 0,942 µm.
d. From the Stapleton sounding analysis.

is probably due to departure of the actual profiles from the exponential form used for the model.

6. Applications to Outdoor PV Testing

A plot of aerosol transmission ($\mathscr{T}$) at 0,500 µm versus diffuse-to-global (horizontal surface) photon flux density ratio (SHGH) over the 0,4 µm to 0,7 µm pass
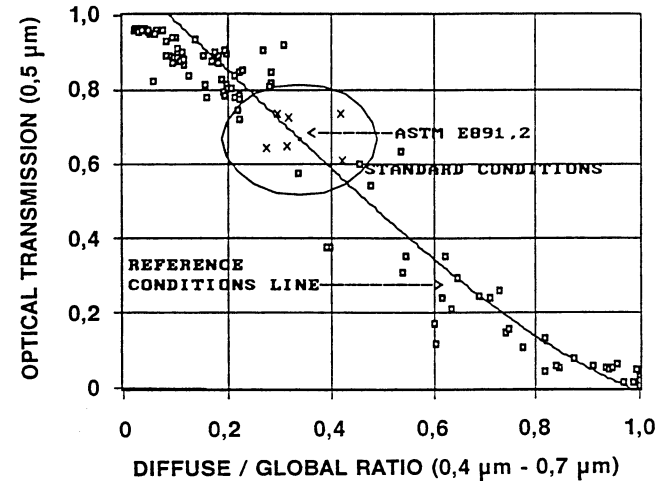
Figure 4. Optical transmission at 0,5 µm versus SHGH in the PWV = 1,42 plane. The line represents values calculated from atmospheric transmission theory, the dot at (0,33, 0,67) corresponds to ASTM #891, 892 standard testing conditions for outdoor PV testing, the circle represents the AOCS parameter limit $(\Delta) = 0,15$.

band is shown in Figure 4. In the figure, the curved (reference conditions) line represents average modelled data under cloud-free conditions over a wide range of transmission $(0 \leq \mathscr{T} \leq 1)$ and RAM $(1 \leq RAM \leq 6)$ values. The dot within the circle corresponds to ASTM 891, 892 standard conditions for testing PV devices [18, 19] − specifically, transmission 0,67 at RAM 1,5. The ASTM standards also specify a PWV (reference) value of 1,42 cm; the plot may be thought of as being the 1,42 cm plane with a PWV axis normal to the figure and passing through the origin.
We now define three δ_i values:

$$\delta_1 = \mathscr{T}_{meas} - \mathscr{T}_{ref}$$
$$\delta_2 = SHGH_{meas} - SHGH_{ref}$$
$$\delta_3 = \beta(PWV_{meas} - PWV_{ref}),$$

representing the differences between the measured (meas) values and reference (ref) values. The β coefficient is used to give PWV appropriate weighting relative to $\mathscr{T}$ and SHGH; β is assumed to be 0,11 for this study.

Taking the root-sum-square of these, we obtain the AOCS coefficient

$$\Delta = \sqrt{\sum_{k=1}^{3} \delta_k^2}.$$ (9)

These relationships are shown graphically in Figure 5. Under reference conditions, $\Delta = 0$. PV performance
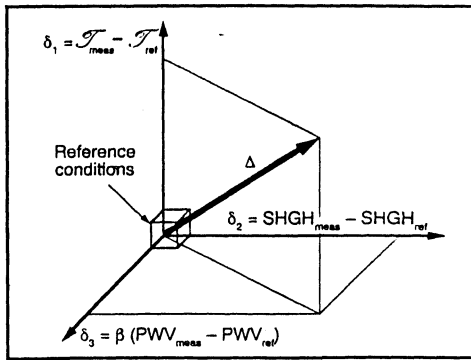

Figure 5. The AOCS parameter Δ is the vector addition of the SHGH, $\mathscr{T}$ and PWV components; β is a coefficient to give δPWV appropriate weighting relative to the other components.

data were taken concurrently with the AOCS on two, not state-of-the-art, amorphous silicon (a-Si) solar modules under a variety of sky conditions, ranging from clear to very cloudy. Identical a-Si total-area efficiency (TAE) data taken concurrently with the AOCS data of Figure 4 are shown in Figures 6 and 7.
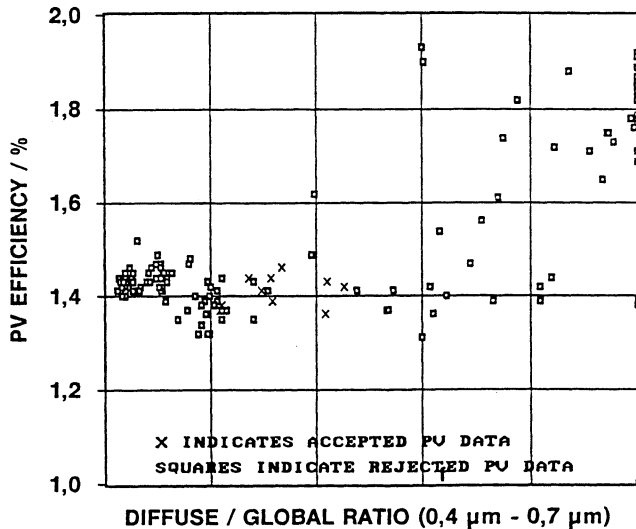
Figure 6. a-Si efficiency versus SHGH for the data of Figure 4. The points marked X represent data for $\Delta \leqq 0,15$, the squares $\Delta > 0,15$ and $\beta = 0$ (i.e. PWV component ignored). See Table 8.

For the data shown in Figure 6, the radius of the circle around the ASTM standard-conditions point shown in Figure 4 is an assumed limiting value of Δ – i.e. PV data are rejected if the AOCS measurements are outside the circle (identified by squares), or accepted (identified by Xs) if inside, based on $\mathscr{T}$ and SHGH only. In Figure 7, the PWV component has been added; the circle of Figure 4 now represents
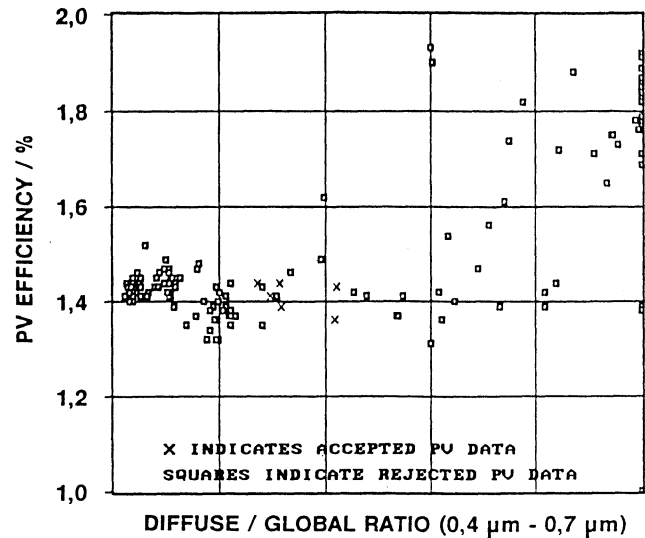
Figure 7. Same as Figure 6, but $\beta = 0,11$ (i.e. PWV component included). See Table 8.

the cross-section of a sphere of radius Δ, and additional points are rejected because they are outside the sphere's radius. A summary of the analysis of two a-Si modules is shown in Table 8.

The fifth column is the product of S, the standard deviation on the random variation of TAE, and t, the two-tailed Student's t values for the 95 % confidence level from [14]. Note the reduction in St of up to 62 % for the low-efficiency case, and up to 79 % for the high-efficiency case, by use of AOCS analysis.

We conclude that the AOCS can be used to reduce variability in outdoor PV test data by monitoring for acceptable atmospheric optical conditions.

7. Additional Applications

In addition to the PV applications, other applications naturally include measurements of the atmospheric optical properties *per se*, including the measurement of spectral aerosol optical depth at selected wavelengths, water vapour and visibility. The spectral aerosol optical depth can be used to estimate the size distribution of suspended aerosol in the atmosphere (see [20]). Under small Δ conditions, AOCS data can be entered into atmospheric spectral transmission models to generate approximate spectra over the solar region. Because of its relative simplicity, reliability, low cost and rugged construction compared with spectroradiometric instruments, the AOCS would be cost effective if deployed to many locations to take routine data of atmospheric optical parameters.

Table 8. AOCS reduction of PV data.

Solar module material	AOCS parameter	Air mass range	Average TAE	S_t	Number of accepted points
Low-efficiency a-Si	No constraints	1 to 4	1,58	0,388	283
Low-efficiency a-Si	No constraints	<1,3	1,54	0,386	177
Low-efficiency a-Si	$\Delta = 0,15$ $\beta = 0$	<1,3	1,44	0,149	12
Low-efficiency a-Si	$\Delta = 0,15$ $\beta = 0,11$	<1,3	1,44	0,159	7
High-efficiency a-Si	No constraints	1 to 4	3,23	0,494	218
High-efficiency a-Si	No constraints	1,4 to 1,7	3,42	0,332	33
High-efficiency a-Si	$\Delta = 0,15$ $\beta = 0$	1,4 to 1,7	3,42	0,267	7
High-efficiency a-Si	$\Delta = 0,15$ $\beta = 0,11$	1,4 to 1,7	3,42	0,105	4

8. Conclusion

The AOCS is proving to be a useful instrument for characterizing local atmospheric optical properties in real time, with application to PV outdoor measurements. By using the SLCF and statistical processing of Langley plot data, the quality of the direct-beam data can be very high. We have described here the instrumentation, measured parameters, calibration, and several practical applications of the AOCS. Additional information on this instrument may be found in [21-24].

References

1. Riordan C. J., *Solar Cells*, 1986, **18**, 223-232.
2. Curtis H. B., *Effect of Atmospheric Parameters on Silicon Cell Performance*, NASA Tech. Rep. CP-2010, 1976.
3. Dave J. V., *Solar Energy*, 1978, **21**, 264-271.
4. Chambouleyron I., Alvarez F., *Proc. 18th IEEE PV Specialists' Conf.*, Las Vegas, NV, 1985, 10/21-25, 533-538.
5. Matson R. J., Emery K. A., Bird R., *Solar Cells*, 1984, **11**, 105-145.
6. Osterwald C. R., *Solar Cells*, 1986, **18**, 171-177.
7. Nann S., Emery K., *Solar Energy Materials and Solar Cells*, 1992, **27**, 189-216.
8. Hulstrom R., Cannon T., *Solar Cells*, 1987, **21**, 329-335.
9. US Patent #4779980 'Atmospheric Optical Calibration System, issued to Hulstrom et al., 25 October 1988.
10. Iqbal M., *An Introduction to Solar Radiation*, New York, Academic Press, 1983.
11. World Meteorological Organization, *Report of Second WMO Expert Meeting on Turbidity Measurement*, Boulder, Colorado, 24-27 October 1978.
12. Leckner B., *Solar Energy*, 1978, **20**, 143-150.
13. Shaw G. E., Reagan J. A., Herman M., *J. Appl. Met.*, 1973, **12**, 374-380.
14. *Uncertainty Measurements Instruments and Apparatus*, Part 1, ASTM Standard PTC 19.1-1985, New York, American Society of Mechanical Engineers, 1986.
15. Hulstrom R. L., *Solar Resources*, Cambridge, MA, MIT Press, 1989, 408 p.
16. McClatchey R. A., Fenn R. W., Selby J. E. A., Volz F. E., Garing J. S., *Optical Properties of the Atmosphere*, 3rd ed., United States Air Force, 1972, 411 p.
17. Press W. H., Flannery B. P., Teukolsky S. A., Vettering W. T., *Numerical Recipes: The Art of Scientific Computing*, Cambridge, Cambridge University Press, 1986, 818 p.
18. American Society for Testing and Materials, *Annual Book of ASTM Standards*, 1987, Section 12, **12.02**, 673-680.
19. American Society for Testing and Materials, *Annual Book of ASTM Standards*, 1987, Section 12, **12.02**, 681-688.
20. Mohamed A. B., Frangi J. P., Fontan J., Druilhet A., *J. Appl. Met.*, 1992, **31**, 1286-1294.
21. Cannon T. W., *Proc. 14th Symp. Photonic Measurements*, SPIE, Bellingham, Wash., 1992.

22. Hulstrom R. L., Cannon T. W., Riordan C. J., Photovoltaic Advanced Research and Development Project, *Solar Radiation Annual Report for 1 October 1986 – 30 September 1987*, SERI/PR-215-3297, 1988.
23. Riordan C. J., Hulstrom R. L., Cannon T. W., Stoffel T. L., Myers D. R., Photovoltaic Advanced Research and Development Project, *Solar Radiation Annual Report for 1 October 1987 – 30 September 1988*, SERI/PR-215-3445, 1989.
24. Hulstrom R. L., Riordan C. J., Cannon T. W., Photovoltaic Advanced Research and Development Project, *Solar Radiation Annual Report for 1 October 1989 – 30 September 1990*, SERI/TP-215-4063, 1990.